

Observational Constraints on Disk Heating as a Function of Hubble Type

Kristen L. Shapiro¹

Department of Astronomy, Williams College, Williamstown, MA 01267, USA

Joris Gerssen, Roeland P. van der Marel

Space Telescope Science Institute, 3700 San Martin Drive, Baltimore, MD 21218, USA

¹Also summer student and visitor at Space Telescope Science Institute

ABSTRACT

Current understanding of the secular evolution of galactic disks suggests that this process is dominated by two or more “heating” mechanisms, which increase the random motions of stars in the disk. In particular, the gravitational influence of giant molecular clouds and irregularities in the spiral potential have been proposed to explain the observed velocity dispersions in the solar neighborhood. Each of these mechanisms acts on different components of the stellar velocities, which affects the ratio σ_z/σ_R of the vertical and radial components of the stellar velocity dispersion since the relative strengths of giant molecular clouds and spiral irregularities vary with Hubble type. A study of σ_z/σ_R as function of Hubble type has the potential to provide strong constraints on disk heating mechanisms. We present major and minor axis stellar kinematics for four spiral galaxies of Hubble type from Sa to Sbc, and use the data to infer the ratios σ_z/σ_R in the galaxy disks. We combine the results with those for two galaxies studied previously with the same technique, with Milky Way data, and with estimates obtained using photometric techniques. The results show that σ_z/σ_R is generally in the range 0.5–0.8. There is a marginally significant trend of decreasing σ_z/σ_R with advancing Hubble type, consistent with the predictions of disk heating theories. However, the errors on individual measurements are large, and the absence of any trend is consistent with the data at the 1- σ level. As a byproduct of our study, we find that three of the four galaxies in our sample have a central drop in their stellar line-of-sight velocity dispersion, a phenomenon that is increasingly observed in spiral galaxies.

Subject headings: galaxies: fundamental parameters — galaxies: kinematics and dynamics — galaxies: individual: NGC 1068, NGC 2460, NGC 2775, NGC 4030

1. Introduction

As cosmological simulations of galaxy formation are becoming increasingly powerful, it has become apparent that these models face their most stringent tests when compared with disk galaxies (e.g., Navarro & Steinmetz 2000). While data vs. N-body model comparisons are currently still restricted to global properties and scaling laws (e.g., Tully-Fisher), it will soon become possible to make more detailed comparisons. In order to constrain these models, it is necessary to have a detailed understanding of the internal dynamics of disk galaxies.

Observationally, the dynamical history of a galactic disk can be probed through the velocity distribution of its constituent stars. In the solar neighborhood, where the three-dimensional distribution of stellar motions can be observed directly, it has long been established that the stellar velocity dispersions correlate with stellar age (i.e., spectral type). Here, the dispersions are observed to vary from about $\sim 10 \text{ km s}^{-1}$ for the earliest spectral type stars to several tens of km s^{-1} for the latest type stars (e.g., Wielen 1977; Dehnen & Binney 1998). This increase in random motion over the lifetime of a star is often referred to as “disk heating” and is attributed to scattering processes. Spitzer & Schwarzschild (1951) identified giant molecular clouds as a scattering source while Barbanis & Woltjer (1967) recognized that stars are also perturbed by irregularities in the potential associated with spiral arms. The former of these mechanisms increases the velocity dispersions isotropically, while the latter primarily increases the dispersions in the plane of the disk. Consequently, different combinations of spiral structure and molecular clouds lead to different relative amounts of heating in the radial and vertical directions of a galactic disk. This was demonstrated explicitly by Jenkins & Binney (1990) using numerical simulations.

Disk heating can be quantified by what is known as the velocity ellipsoid. Schwarzschild (1907) showed that the stellar velocities in the solar neighborhood are well described by a trivariate Gaussian distribution. Since the velocity dispersions near the sun are observed to obey $\sigma_R > \sigma_\phi > \sigma_z$, Schwarzschild’s distribution has an ellipsoidal shape in velocity space. The exact shape of this ellipsoid is defined by its two axis ratios, σ_z/σ_R and σ_ϕ/σ_R . (The orientation of the velocity ellipsoid is set by the cross-terms σ_{Rz} and $\sigma_{R\phi}$, which, in the plane of the disk, are both zero for a stellar population that is distributed symmetrically.) In an axisymmetric disk with stellar orbits not too far from circular (the epicycle approximation), σ_ϕ/σ_R depends only on the circular velocity and not on any disk heating mechanism. Measurements of the ratio σ_z/σ_R therefore constrain the heating processes in galactic disks.

The dependence of disk heating on the relative amount of molecular gas and spiral structure suggests that the velocity ellipsoid ratio σ_z/σ_R should vary as a function of Hubble type, since both molecular gas content and morphology are functions of Hubble type. This hypothesis was first tested by Gerssen et al. (1997, 2000), who developed a method for measuring all three components of the stellar velocity dispersions in external galaxies. Their application of this technique to NGC 488 (Sb) and NGC 2985 (Sab) showed that the derived ratios in these systems are consistent with the trend seen in simulations by Jenkins & Binney (1990). The same is true for the Milky Way (Sbc). However, for the external galaxies, the errors on each individually-determined velocity ellipsoid ratio are rather large, since galactic disks are characterized by low surface brightness and by relatively small internal velocity dispersions. Rather than try to reduce the errors on individual

points, we attempt here to improve the statistics on a possible relation with Hubble type by applying the technique of Gerssen et al. to four additional disk galaxies. The inclusion of these data both triples the sample of galaxies with direct measurements of the stellar velocity ellipsoid ratio and expands the sampled range of morphological types.

2. Method

In an intermediate-inclination galaxy, spectra obtained along radius vectors with different position angles will probe different projections of the velocity ellipsoid. The velocity dispersions along an arbitrarily positioned spectrum in a thin axisymmetric disk can be expressed as

$$\sigma_{\text{los}}^2 = [\sigma_R^2 \sin^2 \theta + \sigma_\phi^2 \cos^2 \theta] \sin^2 i + \sigma_z^2 \cos^2 i, \quad (1)$$

where i is the inclination angle of the galaxy and θ is the position angle with respect to the major axis in the plane of the disk. In this equation, there are three unknown quantities (σ_R , σ_ϕ , and σ_z), but σ_ϕ/σ_R is constrained by the epicycle approximation (see below). Hence, there are two independent unknowns in this equation, and observations along at least two axes are required to extract both (Gerssen et al. 1997). Maximum leverage is obtained by taking spectra along the major axis, where the line-of-sight stellar velocity dispersions are a combination of σ_ϕ and σ_z , and along the minor axis, where they are a combination σ_R and σ_z . In an axisymmetric disk, the stellar velocities along any third axis will simply be a linear combination of these two and will not provide additional information.

Assuming that most orbits in disk galaxies are well-described by the epicycle approximation, the dispersions in the azimuthal and radial direction are related according to

$$\frac{\sigma_\phi^2}{\sigma_R^2} = \frac{1}{2} \left(1 + \frac{\partial \ln V_c}{\partial \ln R} \right), \quad (2)$$

where V_c is the circular speed in the galaxy. This equation, together with the observations along the major and minor axes, fully constrains the velocity ellipsoid ratio σ_z/σ_R . This model is illustrated in Figure 1, in which the predicted major to minor axis velocity dispersion ratio $\sigma_{\text{major}}/\sigma_{\text{minor}}$ is plotted against the velocity ellipsoid ratio σ_z/σ_R for a variety of inclinations under the assumption of a flat rotation curve ($V_c = \text{constant}$). In principle, any value of σ_z/σ_R can be obtained using this method, but disk heating theories as well as solar neighborhood observations suggest that this ratio, in practice, does not exceed unity.

When direct measurements of the circular speed are available (e.g. from an emission-line rotation curve), this information can be included in equation (2). Otherwise, V_c must be estimated from the stellar rotation curve $\bar{V}(R)$ through the asymmetric drift equation,

$$V_c^2 - \bar{V}^2 = -R \frac{\partial \sigma_{Rz}}{\partial z} + \sigma_R^2 \left[\frac{R}{h} - R \frac{\partial}{\partial R} \ln(\sigma_R^2) - \frac{1}{2} + \frac{R}{2V_c} \frac{\partial V_c}{\partial R} \right], \quad (3)$$

where h is the photometric disk scale length and σ_{Rz} measures the tilt of the velocity ellipsoid in the (R, z) plane. The tilt term $R \frac{\partial \sigma_{Rz}}{\partial z}$ is always between 0 and $(\sigma_R^2 - \sigma_z^2)$ (Binney & Tremaine

1987). (Orbit integration by Binney & Spergel (1983) and Kuijken & Gilmore (1989), see also Kent & de Zeeuw (1991), suggests that the solar neighborhood value is midway between these two extremes.) Substitution of these two limiting cases of the tilt term into the model does not produce significantly different results (Gerssen et al. 1997). For the present study, this term was set to zero without loss of generality. When both gas and stellar rotation curves are available, the system is overdetermined, and the asymmetric drift equation can function either as a consistency check on the derived model velocities or as an additional constraint to more consistently fit all the available data.

Although the functional forms of all the variables can be directly determined using the above equations, this method is very sensitive to noise (Merrifield & Kuijken 1994). Instead, we adopt a model-fitting approach. We assume that, at the radii where the disk light dominates, the circular velocity can be described by a power law,

$$V_c = V_{c,0} R^\alpha. \quad (4)$$

The other two observables, σ_{major} and σ_{minor} , are modeled assuming exponential distributions for both the radial and the vertical dispersion components.

$$\sigma_R = \sigma_{R,0} e^{-R/h_{\text{kin}}}, \quad (5)$$

$$\sigma_z = \sigma_{z,0} e^{-R/h_{\text{kin}}}. \quad (6)$$

Although there is no a priori reason to assume that the kinematical scale length, h_{kin} , should be the same for both the radial and the vertical component, the quality of our data is insufficient to constrain both of these parameters independently.

3. Observations and Data Reduction

3.1. Spectroscopy

Observations were carried out on January 12–15, 2002 at the Mayall 4-meter telescope at the Kitt Peak National Observatory. We observed four galaxies: NGC 1068, NGC 2460, NGC 2775, and NGC 4030. All four are nearby, spiral galaxies of intermediate inclination ranging in Hubble type from Sa to Sbc. The main characteristics of each galaxy are listed in Table 1.

Long-slit spectra were obtained along the photometric major and minor axes of each galaxy, in multiple exposures of 30 minutes each. The orientation and position of each slit is shown schematically in Figure 2, and the log of the observations is reported in Table 2. Spectra of several late-G and early-K giant stars were also acquired to serve as templates in the stellar kinematical analysis. All data were taken with the Ritchey-Chretien Focus Spectrograph using the KPC-24 grating in second order, centered on the Mg b absorption feature at ~ 5175 Å, which yielded a velocity scale of 30 km s^{-1} per pixel on the T2KB CCD. The spatial scale of this configuration is 0.69 arcsec/pixel. The long-slit spectra (5.4 arcmin long) were obtained with a 3.0 arcsec wide slit. Seeing conditions varied during the observations but were fairly poor, ~ 1.5 arcsec. However,

our kinematical analysis of the data focuses on smooth kinematical gradients at large radii, and poor spatial resolution is therefore not a problem. Calibration arc spectra obtained with a FeAr lamp were taken every 30 minutes.

The data were reduced using the standard IRAF² packages. Each exposure was overscan- and bias-subtracted, corrected for pixel-to-pixel variations using internal lamp exposures, and corrected for large scale gradients and vignetting using sky frames obtained in evening or morning twilight. The arc lamp frames were used to wavelength-calibrate and spatially rectify the spectra. All spectra were rebinned onto a logarithmic wavelength scale to facilitate the kinematical analysis. Finally, all spectra were sky subtracted using data near the edges of the slit.

In each galaxy spectrum, rows along the spatial direction were co-added to increase the signal-to-noise ratio. These co-added bins ranged in size from one pixel in the center of a galaxy to ~ 20 pixels at large radii. For the stellar template spectra, the relevant rows along the slit were combined to create one-dimensional stellar spectral profiles.

3.2. Photometry

In addition to the spectroscopic data, we obtained photometric data from several archives. For NGC 2460 and NGC 4030, *HST*/WFPC2 images in filter F814W were obtained from the *HST* archive. Archived *K* band images were obtained for NGC 1068 (2MASS) and NGC 2775 (Mollenhoff & Heidt 2001). After sky subtraction, the azimuthally averaged surface brightness profiles were extracted for each galaxy using the stsdas task ELLIPSE in IRAF. The results are illustrated in Figure 2.

At large radii, all four of the galaxies exhibit exponential disks, the scale lengths of which are found by simply fitting a line to this part of the surface brightness profile. Furthermore, subtraction of the linear fit from the profile shows the radii at which light from the bulge dominates that of the galaxy. At these radii, the derived stellar velocities are a measure of the bulge kinematics and not of the disk kinematics. Kinematical data points obtained at these radii were therefore excluded from the modeling. Estimates of the inclination of each galaxy were also found in the isophotal fitting procedure. The derived quantities are reported and compared to literature values in Table 1.

4. Kinematical Analysis

4.1. Absorption Lines

Stellar velocity dispersions were extracted from the reduced spectra using the standard assumption that the observed galaxy spectrum is the convolution of a Gaussian velocity

²IRAF is the Image Analysis and Reduction Facility distributed by the National Optical Astronomy Observatories.

distribution and a typical stellar (template) spectrum. We did not attempt to extract higher-order moments of the velocity distributions after a preliminary analysis revealed no significant departures from a single Gaussian.

The Gaussian that best fits the galaxy data in a least-squares sense yields the mean stellar line-of-sight velocities and the stellar velocity dispersions. We derived the stellar kinematics using two independent methods, one of which performs the least square minimization in pixel space (van der Marel 1994) and the other of which does this task in Fourier space (using software originally developed by Konrad Kuijken). The results derived from both methods were found to be in good agreement. The analysis was repeated with each template star. Different template stars did not yield significantly different results and we therefore did not attempt to construct an optimal template spectrum. Instead, we used the template star that yielded the the marginally best χ^2 value. Three of the four galaxies (NGC 1068, NGC 2460, and NGC 4030) were best modeled by HD55184, of spectral type K0III; the fourth, NGC 2775, was most accurately fit by HD18991, of type G9III. The derived major and minor axis mean stellar velocity and velocity dispersions for each galaxy are shown in Figure 3. The abscissa is the radius in the disk, which for the minor axis was obtained through deprojection.

Although the primary focus of this project is on the outer disk kinematics, we note that three of the four galaxies in our sample show noticeable central drops in their stellar velocity dispersions. Such features are increasingly observed in kinematical studies of both Seyfert and non-active spiral galaxies (Bottema 1989; Emsellem et al. 2001; de Zeeuw et al. 2002; Marquez et al. 2003). This phenomenon is generally attributed to a kinematically decoupled core (Bottema & Gerritsen 1997). Alternatively, Emsellem et al. (2001) suggested that these central dispersion drops are the results of recent star formation in nuclear disks. They note that such a process could be fueled by gas inflow along a nuclear bar. However, the three galaxies in which we detect this phenomenon (NGC 2460, NGC 2775, and NGC 4030) are non-active and are not known to display starburst activity (although such activity may have occurred in the recent past). Other explanations may therefore be necessary to account for the central dispersion drops in these galaxies.

4.2. Emission Lines

The spectral range of the long-slit spectra also included several emission lines, most notably the [OIII] line at 5007 Å. For three of our four galaxies, these [OIII] lines were fitted with a Gaussian profile, using the same spatially co-added bins as for the absorption line data. Due to the Seyfert nature of the fourth galaxy, NGC 1068, the [OIII] line is completely saturated in our spectra. Instead, for this galaxy we used the [NI] doublet at 5199 Å. The two emission lines in this feature were each fitted simultaneously with a Gaussian profile and the combined fit accurately matched both of the emission lines. The wavelength shift between the two Gaussians was kept fixed since we assume that both lines trace the same kinematics.

Since the velocity dispersions of gas in disks is typically $\lesssim 10 \text{ km s}^{-1}$, the rotation curves derived in this manner provide a direct estimate of the circular velocities of the galaxies. The

major axis gas rotation curves are overplotted on the stellar rotation curves in Figure 3. Except for NGC 4030, the asymmetric drift (i.e. the difference between the gas and the stellar velocities) is clearly noticeable. Apparently, the gas in NGC 4030 is not an accurate tracer of the circular velocity in this system. Also unusual is the central feature in the gas kinematics of NGC 1068, which is most likely due to the bar and complicated structure in the nucleus of this system (Scoville et al. 1988). At larger radii, however, the gas kinematics for this galaxy are quite regular.

5. Modeling

We used the model described in Section 2 to simultaneously fit the three observables, σ_{major} , σ_{minor} , and $\bar{V}(R)$. The five best-fit model parameters, $\sigma_{R,0}$, $\sigma_{z,0}$, h_{kin} , $V_{c,0}$, and α were obtained using the non-linear fit routines of Press et al. (1992). The inferred parameters for each galaxy are tabulated in Table 3, and the corresponding best model fits are shown in Figure 4 over the range of radii for which the kinematics are dominated by the disk. All results were confirmed using an alternative minimization routine, the downhill simplex method (Press et al. 1992). Error bars on the best-fitting model parameters were determined using bootstrapping.

We examined the dependence of the derived parameters, and in particular the velocity ellipsoid ratio σ_z/σ_R on uncertainties in the input parameters. Within the error ranges on the photometric scale length h and the inclination i quoted in Table 1, changes in the values of these two parameters do not significantly affect the final results. We also tested the dependence on position angle by assuming that the true major axis is offset from our observed major axis by ΔPA degrees. We then reran the models and found that mismatches of up to 25 degree in the adopted major axis position angle do not significantly affect the velocity ellipsoid ratio at a level beyond ~ 0.1 . As is evident from the major and minor axis rotation curves in Figure 3, none of the galaxies in our sample have major axis position angles that were misidentified by more than ~ 10 degrees.

Observations of edge-on galaxies show that the scale height of a disk is generally independent of distance from the galaxy center and that the vertical surface brightness distribution can be fitted with a hyperbolic secant function (e.g. van der Kruit 1989). The isothermal sheet approximation, together with these observations implies that the vertical component of the stellar velocity dispersion σ_z should decline exponentially with radius with a kinematical scale length h_{kin} that is twice the photometric scale length h . However, in our model fits we do not generally find kinematical scale lengths that obey this relation. So most likely the assumptions on which $h_{\text{kin}} = 2h$ is based do not hold in these galaxies (or in general).

In the following sections, details of the modeling procedure for each galaxy are described.

5.1. NGC 1068

NGC 1068 is one of the prototypical Seyfert galaxies. Its central structure is quite complex. High spatial resolution CO observations (Schinnerer et al. 2000) show both a central bar and central spiral arms. The central feature in our emission line rotation curve (Figure 3, panel a) is another manifestation of the central complexity in this system. However, at larger radii the morphology is similar to that of a regular Sb galaxy. As the brightest and nearest of the four galaxies in our sample, NGC 1068 has the most extensive stellar kinematical data set of the four galaxies. Its kinematics are accurately fit by the model. In contrast, the gas kinematics are more erratic and are measured to smaller radial extent, but they are not inconsistent with the circular velocities predicted from the stellar rotation curve using equation (3) (dotted line in Figure 4). Kaneko et al. (1992), using several optical emission lines, derive a gas rotation curve that corresponds closely to the model prediction of $V_{c,0}$. The best-fit model has velocity ellipsoid axis ratio $\sigma_z/\sigma_R = 0.58 \pm 0.07$.

As shown in Figure 2, the large radial extent of NGC 1068 dictates that the diameter of the galaxy along the major axis is somewhat longer than the slit length. However, near the slit ends, the night sky completely dominates the underlying galaxy light, and this part of the slit is therefore very effective in subtracting the sky background. Indeed, our kinematical spectral modeling provided no evidence of residual night sky contamination.

5.2. NGC 2460

Panel (b) in Figure 3 shows that the amplitudes of the stellar rotation curves on the two opposite sides of NGC 2460 are somewhat different. This disparity is probably related to a significant asymmetry in the galaxy's HI distribution (Haynes et al. 1998). As the only Sa type galaxy in our sample, NGC 2460 has a relatively large bulge, which means that much of our kinematical data were discarded on the grounds that they are dominated by the bulge kinematics. This left few disk data points, especially along the minor axis. To compensate for these limitations, we tried including the gas kinematics in the model fit as a constraint on the circular velocity (instead of predicting $V_c(R)$ from $\bar{V}(R)$ using equation 3). We also tried separate fits using data sets that included only one or both sides of the stellar rotation curve. There is considerable scatter in the individual fits, and the velocity ellipsoid ratio σ_z/σ_R is therefore not very precisely determined for NGC 2460. We find $\sigma_z/\sigma_R = 0.83 \pm 0.35$, with the large error bar representing the scatter among the results of the different ways of performing the data-model comparison. Observations of the rotation curve of NGC 2460 by Marquez et al. (2002), when deprojected, yield a circular speed of approximately 210 km s^{-1} . This compares well to our observations, which suggest a similar value, and to our model fit of $218 \pm 24 \text{ km s}^{-1}$.

5.3. NGC 2775

Most often classified as either Sa or Sab, NGC 2775 has a large bulge whose exact extent is a matter of some debate in the literature (see below). To best fit the kinematics of this galaxy, we assumed a flat rotation curve, as has been observed to large radii by Rubin et al. (1985) and Corsini et al. (1999). Figure 4 shows the result obtained under this assumption. The models are able to fit most data except for the major axis dispersions at the largest radii (which remain rather flat and therefore try to push the kinematical scale length to infinity). The derived value of the velocity ellipsoid axis ratio is $\sigma_z/\sigma_R = 1.02 \pm 0.11$.

Rubin et al. (1985) and Corsini et al. (1999) both find the circular speed to be $\sim 310 \text{ km s}^{-1}$, a value that is somewhat higher than our measured gas velocity of $\sim 280 \text{ km s}^{-1}$. As our circular speed was derived using a fairly weak [OIII] line (while the literature values were obtained with higher signal-to-noise), the modeling was rerun with the circular speed forced to coincide with the literature quantities. This change did not alter the results significantly.

Comparison of the photometric analysis described in Section 3.2 with the literature revealed that the bulge-disk transition radius of NGC 2775 is a value of much debate (see Boroson 1981; Grosbol 1985; Moriondo et al. 1998; Mollenhoff & Heidt 2001). The two most recent decompositions, done using K band data by Moriondo et al. and by Mollenhoff & Heidt, disagree significantly. The decomposition of Mollenhoff & Heidt concurs with those of Boroson (1981) and Grosbol (1985) in concluding that the disk dominates the galactic light only outwards of ~ 70 arcsec. In contrast, Moriondo et al. quote an effective bulge radius of only 14 arcsec. This last result resembles that found in this project, which restricts the bulge's influence to the inner 30-40 arcsec of the galaxy. Given the disparity in the literature, the possibility exists that the bulge dominates the dispersions even at radii where we assumed them to be disk dominated. Since bulges of galaxies are believed to be roughly isotropic (Kormendy & Illingworth 1982; Spaenhauer et al. 1992), the inferred velocity ellipsoid ratio σ_z/σ_R must therefore be considered an upper limit.

5.4. NGC 4030

A complication in the modeling of NGC 4030 is the gas rotational velocity, which is similar to that of the stars and which therefore indicates that the gas cannot be rotating at the circular velocity. (The alternative explanation that the stellar rotation in NGC 4030 is close to the circular velocity is unlikely since the observed stellar velocity dispersions in this system are comparable in magnitude to the dispersions observed in the other galaxies in the sample.) This may result from the gas not being in an equilibrium state at present or from the gas not being characterized by circular orbits, either of which could be the result of a recent interaction. Either way, the gas kinematics of this galaxy can clearly not be included to help constrain our models. We therefore fitted the model to the stellar data to obtain $\sigma_z/\sigma_R = 0.64 \pm 0.28$. The stellar kinematics are well fitted by the model, but the predictions for the circular velocity are larger than the observed gas kinematics, as expected. The large error on the velocity ellipsoid ratio reflects the relatively low data quality for the minor axis data, the observations of which were affected by reduced

transmission due to clouds. The total integration time along this axis is effectively only half as much as for the major axis observations.

The only literature measurement of the gas kinematics in this galaxy is that of Mathewson & Ford (1996), who measured the maximum rotational velocity of the gas and found a value of 236 km s^{-1} . This is similar to the rotational speed of our data, which, when deprojected, is $\sim 230 \text{ km s}^{-1}$. Both of these values, however, coincide with stellar velocities and so are lower than the predicted circular speed of 263 km s^{-1} .

6. Results

Combining the velocity ellipsoid axis ratios derived here with the other two direct measurements of this value for external galaxies (Gerssen et al. 1997, Gerssen et al. 2000) and with the value for the Milky Way yields the result shown in Figure 5. This graph represents the first direct investigation of the velocity ellipsoid ratio as a function of morphological type.

In addition to these kinematical results, van der Kruit & de Grijs (1999) present an alternative method of constraining the ratio of the velocity ellipsoid. Their approach is based on photometric observations of edge-on galaxies and therefore relies on a number of assumptions in order to link the photometry to a kinematical quality. The velocity ellipsoid ratios derived using this technique are presented as averages over all the galaxies of a particular Hubble type (where the sample ranges from Sb to Sd). The earliest types in their sample have average ratios that agree well with our individually-determined ratios in the same bins.

The strength of the trend of velocity ellipsoid ratio with Hubble type was assessed both for the set of direct measurements of this value (solid points in Figure 5) and for all available data (solid and open points). Linear regressions that account for both horizontal and vertical errors were performed. The fit to the set of direct measurements of the velocity ellipsoid axis ratio has a slope of -0.11 ± 0.08 . Van der Kruit and de Grijs observed no obvious trend in their data (open symbols). Linear regression of the combined results of their study with those of this paper indicate a slope of -0.05 ± 0.04 . For both regressions the goodness-of-fit is statistically acceptable and the data marginally suggest a downward trend in the ratio σ_z/σ_R with advancing Hubble type. However, this is significant only at the one sigma level, and the absence of any trend is not ruled out by the available data.

7. Discussion and Conclusions

The fits described in Section 5 show that modeling each of the galaxies in our sample is not without difficulties, despite the optically regular-looking morphologies of the galaxies. Problems include the asymmetric rotation curve of NGC 2460 and the fact that the gas velocities in NGC 4030 probably do not trace the circular velocity. To some extent this may simple reflect the real nature of galaxies. For example, early results from the SAURON survey of elliptical galaxies

show (de Zeeuw et al. 2002) that a regular appearance alone is no guarantee of regular stellar kinematics.

The results derived here are qualitatively consistent with the implicit predictions of Jenkins and Binney (1990), who attribute secular evolution in disk galaxies to a combination of spiral irregularities and encounters with GMCs. They express the relative importance of these two mechanisms with a parameter β , and their simulations indicate that increasing β (increasing the importance of spiral structure) results in smaller σ_z/σ_R (Jenkins & Binney 1990). For the solar neighborhood, they use the observed shape of the velocity ellipsoid and the velocity dispersion-age relation to conclude that $\beta \sim 90$.

To estimate the relative importance of GMCs in the different galaxies of our sample we used the FCRAO extragalactic CO survey (Young et al. 1995). The H₂ surface densities (Table 4) were derived assuming a constant CO to H₂ conversion factor. The derived surface densities indicate that the molecular content of the sample galaxies decreases with advancing Hubble type. (The exception to this trend is NGC 1068, in which Young et al. observe both an exponential distribution of gas and a CO ring; this combination makes the mean surface density of H₂ difficult to estimate). Various studies (e.g. Wilson 1995) find that this factor increases as the metallicity of the host galaxy decreases. Using Wilson's expression and an estimate of the metallicity in each galaxy obtained from the observed correlation between metallicity and absolute magnitude (Roberts & Haynes 1994), we calculate that changes in the conversion factor due to metallicity are less than 10 percent for the galaxies in our sample, except for NGC 1068 where the difference is ~ 20 percent. This is much less than the differences in H₂ density between the galaxies in Table 4, and therefore does not affect the present discussion at a significant level.

The morphological classifications of galaxies imply that the earlier-type galaxies are more tightly wound and more regular (see images in Figure 2). It is therefore quite likely that the spiral potentials associated with earlier-type galaxies are smoother than those of later-types. Combined with the H₂ surface densities in Table 4 this suggests that the earlier-type galaxies have smaller values for β and thus larger σ_z/σ_R ratios. The results of our study are consistent with this prediction and, at 1- σ confidence, confirm it.

An alternative explanation of disk heating is presented by Hanninen and Flynn (2002), who attribute observed heating to the combined influences of GMCs and hypothesized massive halo black holes. Although simulations using these assumptions do account for the solar neighborhood velocity ellipsoid, this need not extend to external galaxies since the dark matter content in these systems is generally not well known. Any further analysis of this possibility awaits observational confirmation of the existence of a significant population of intermediate-mass black holes in the halos of galaxies (see van der Marel 2003 for a review of present observational constraints).

In order to provide more rigorous constraints on theoretical models, additional data is necessary. The technique described here is straightforward and can readily be applied to a larger sample of disk galaxies. Despite the sizable error bars associated with individual galaxies, an increase in sample size could unequivocally establish the presence of the trend suggested by our data. The results presented here are only a first step in the observational investigation that is critical to understanding disk heating. Subsequent work could benefit from the use of Integral

Field Units. IFUs that have a sufficiently large field-of-view and enough spectral resolution to study stellar velocity dispersions ($R \gtrsim 5000$) are ideally suited to extend the sample of galaxies. Kinematical data sets that cover a substantial fraction of a disk will provide both a consistency check on the underlying model assumptions and more precisely determined constraints on the velocity ellipsoid.

We thank Konrad Kuijken for his absorption line analysis program and the referee for useful comments. We are also very grateful to Kitt Peak National Observatory for the use of their facilities and their helpful staff, in particular Bill Gillespie. KLS wishes to thank the Space Telescope Science Institute for repeated hospitality in hosting her as both a summer student and a visitor.

REFERENCES

Baggett, W.E., Baggett, S.M., & Anderson, K.S.J. 1998, AJ, 116, 1626

Barbanis, B., & Woltjer, L. 1967, ApJ, 150, 461

Binney, J., Spergel, D. N., 1983, The Nearby Stars and the Stellar Luminosity Function, IAU Colloquium '76, eds. A. G. D. Philip & A. R. Upgren, Davis Press, p. 259

Binney, J., Tremaine, S. 1987, Galactic Dynamics (Princeton: Princeton University Press)

Boroson, T. 1981, ApJS, 46, 177

Bottema, R. 1989, A&A, 221, 236

Bottema, R., & Gerritsen, J.P.E. 1997, MNRAS, 290, 585

Clemens, D.P., Sanders, D.B., & Scoville, N.Z. 1988, ApJ, 327, 139

Corsini, E.M., et al. 1999, A&A, 342, 671

de Zeeuw, P.T., et al. 2002, MNRAS, 329, 513

Dehnen, W., & Binney, J. 1998, MNRAS, 298, 387

Emsellem, E., Greusard, D., Combes, F., Friedli, D., Leon, S., Pecontal, E., & Wozniak, H. 2001, A&A, 368, 52

Frei, Z., Guhathakurta, P., Gunn, J.E., & Tyson, J.A. 1996, AJ, 111, 174

Garcia-Gomez, C., Athanassola, E., & Barbera, C. 2002, A&A, 389, 68

Gerssen, J., Kuijken, K., & Merrifield, M.R. 1997, MNRAS, 288, 618

Gerssen, J., Kuijken, K., & Merrifield, M.R. 2000, MNRAS, 317, 545

Grosbol, P.J. 1985, A&AS, 60, 261

Hanninen, J., & Flynn, C. 2002, MNRAS, 337, 731

Haynes, M.P., Hogg, D.E., Maddalena, R.J., Roberts, M.S., & van Zee, L. 1998, ApJ, 115, 62

Huchtmeier, W.K., & Richter, O.-G. 1989, A General Catalog of HI Observations of Galaxies (New York: Springer)

Jenkins, A., & Binney, J. 1990, MNRAS, 245, 305

Kaneko, N., Satoh, T., Toyama, K., Sasaki, M., Nishimura, M., & Yamamoto, M. 1992, AJ, 103, 422

Kent, S. M., & de Zeeuw, P. T. 1991, AJ, 102, 1994

Kormendy, J., & Illingworth, G. 1982, ApJ, 256, 460

Kuijken, K., Gilmore, G. 1989, MNRAS, 239, 571

Laurikainen, E., & Salo, H. 2002, MNRAS, 337, 1118

Marquez, I., Masegosa, J., Moles, M., Varela, J., Bettoni, D., & Galletta, G. 2002, A&A, 393, 389

Marquez, I., et al. 2003, A&A, in press (astro-ph/0306497)

Mathewson, D.S., & Ford, V.L. 1996, ApJS, 107, 97

Merrifield, M., & Kuijken, K. 1994, ApJ, 432, 575

Mollenhoff, C., & Heidt, J. 2001, A&A, 368, 16

Moriondo, G., Giovanardi, C., & Hunt, L.K. 1998, A&AS, 130, 81

Naim, A., et al. 1995, MNRAS, 274, 1107

Navarro, J.F., & Steinmetz, M. 2000, ApJ, 538, 477

Press, W.H., et al. 1992, Numerical Recipes: The Art of Scientific Computing (New York: Cambridge University Press)

Roberts, M. S., Haynes, M. P. 1994, ARAA, 32, 115

Roth, J. 1994, AJ, 108, 862

Rubin, V.C., Burnstein, D., Ford, W.K. Jr., & Thonnard, N. 1985, ApJ, 289, 81

Schinnerer, E., Eckart, A., Tacconi, L. J., Genzel, R., & Downes, D. 2000, ApJ, 533, 868

Schwarzschild, K. 1907, in *Göttingen Nachr.*, p.614

Spaenhauer, A., Jones, B.F., & Whitford, A.E. 1992, AJ, 103, 297

Spitzer, L., Schwarzschild, M., 1951, ApJ, 114, 385

van der Kruit, P. C., 1989, The Milky Way as a Galaxy, University Science Books, R. Buser, I. R. King eds.

van der Kruit, P.C., & de Grijs, R. 1999, A&A, 352, 129

van der Marel, R.P. 1994, MNRAS, 270, 271

van der Marel, R. P. 2003 Coevolution of Black Holes and Galaxies, ed. L. C. Ho, (Cambridge: Cambridge Univ. Press), in press (astro-ph/0302101)

Wielen, R. 1977, A&A, 60, 263

Wilson, D. C. 1995, ApJ, 488, L97

Young, J.S., et al. 1995, ApJS, 98, 219

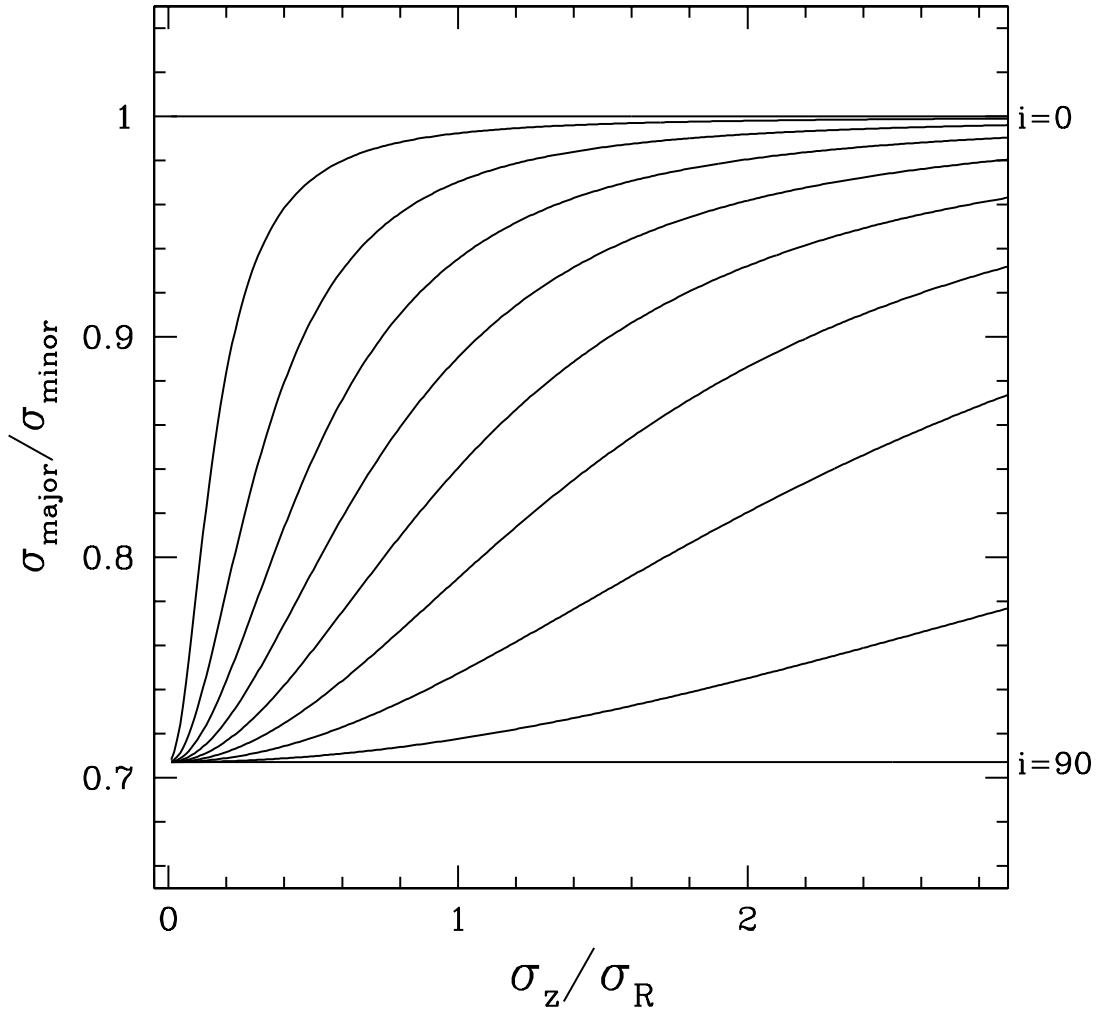


Fig. 1.— Relation of the ratio of the observed major to minor axis dispersions to the velocity ellipsoid ratio σ_z/σ_R , assuming a flat rotation curve. Under this assumption, the major axis dispersions cannot be smaller than $\sqrt{1/2}$ times the minor axis dispersions. The velocity ellipsoid ratio σ_z/σ_R can in principle have any value; however, observations of this ratio in the solar neighborhood and existing disk heating theories suggest that σ_z/σ_R does not exceed unity. Different curves are for inclinations between 0° (face-on) and 90° (edge-on) in steps of 10 degrees.

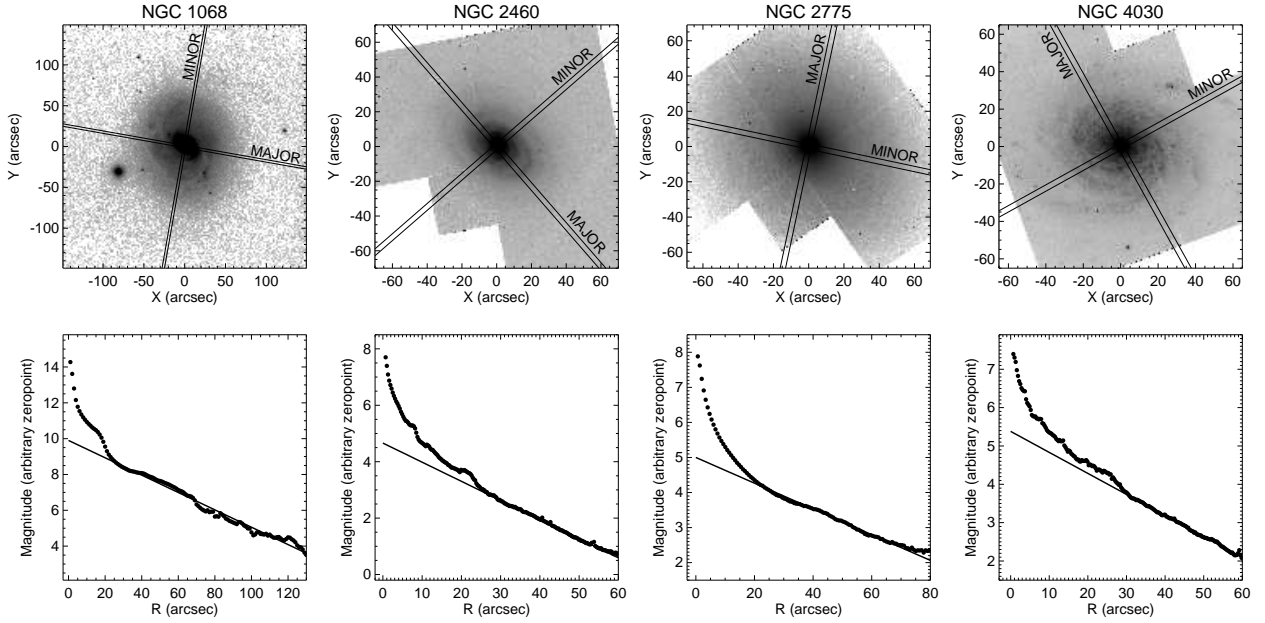


Fig. 2.— Logarithmic grey scale images of the four galaxies in our sample are shown in the top panels. From left to right: NGC 1068 (DSS image), NGC 2460, NGC 2775, and NGC 4030. The last three images are archival *HST*/WFPC2 images obtained with the F814W filter. In each panel, North is at the top and East is to the left. The 5.4 arcmin long-slits positions along which we obtained the spectra are overplotted in each panel. The slits are positioned close to the major and minor axes in each galaxy (see text). The panels on the bottom show the radial surface brightness profiles derived from the images. (For NGC 2460 and NGC 4030, the WFPC2 images shown here were used; for NGC 1068, a 2MASS K band image was used; and for NGC 2775, a K band image acquired by Mollenhoff & Heidt (2001) was used.) The profiles show the extent of the bulge component in each galaxy. The solid lines are exponential fits to the outer disk component. The best-fit exponential scale lengths are in close agreement with literature values (see Table 1).

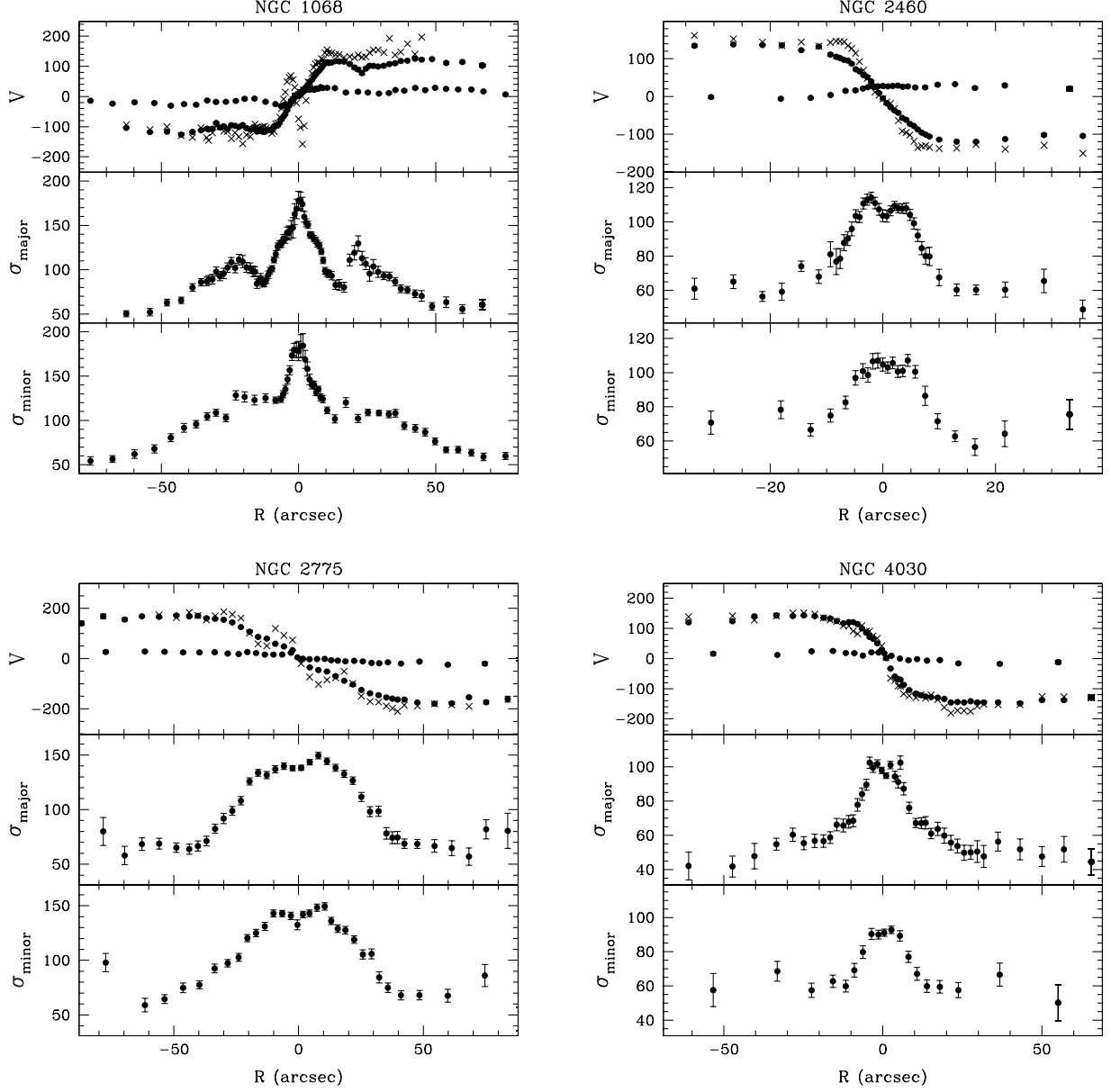


Fig. 3.— Observed kinematics of the four galaxies in our sample: **a: top left** NGC 1068, **b: top right** NGC 2460, **c: bottom left** NGC 2775 and **d: bottom right** NGC 4030. In each panel the kinematical information is given in km s^{-1} . Filled circles represent major and minor axis stellar data; crosses represent gas data. Error bars for the stellar velocities are shown but are generally smaller than the plot symbols. The error bars for the gas velocities are shown in Figure 4. The top panel for each galaxy shows the gas major axis rotation curve, the stellar major axis rotation curve, and the stellar minor axis velocities overplotted (the latter are always near 0 km s^{-1}). The galaxy systemic velocities have been subtracted. The lower two panels for each galaxy show the major and minor axis stellar velocity dispersions respectively. The abscissa is the radius in the disk, which, for the minor axis, was obtained through deprojection.

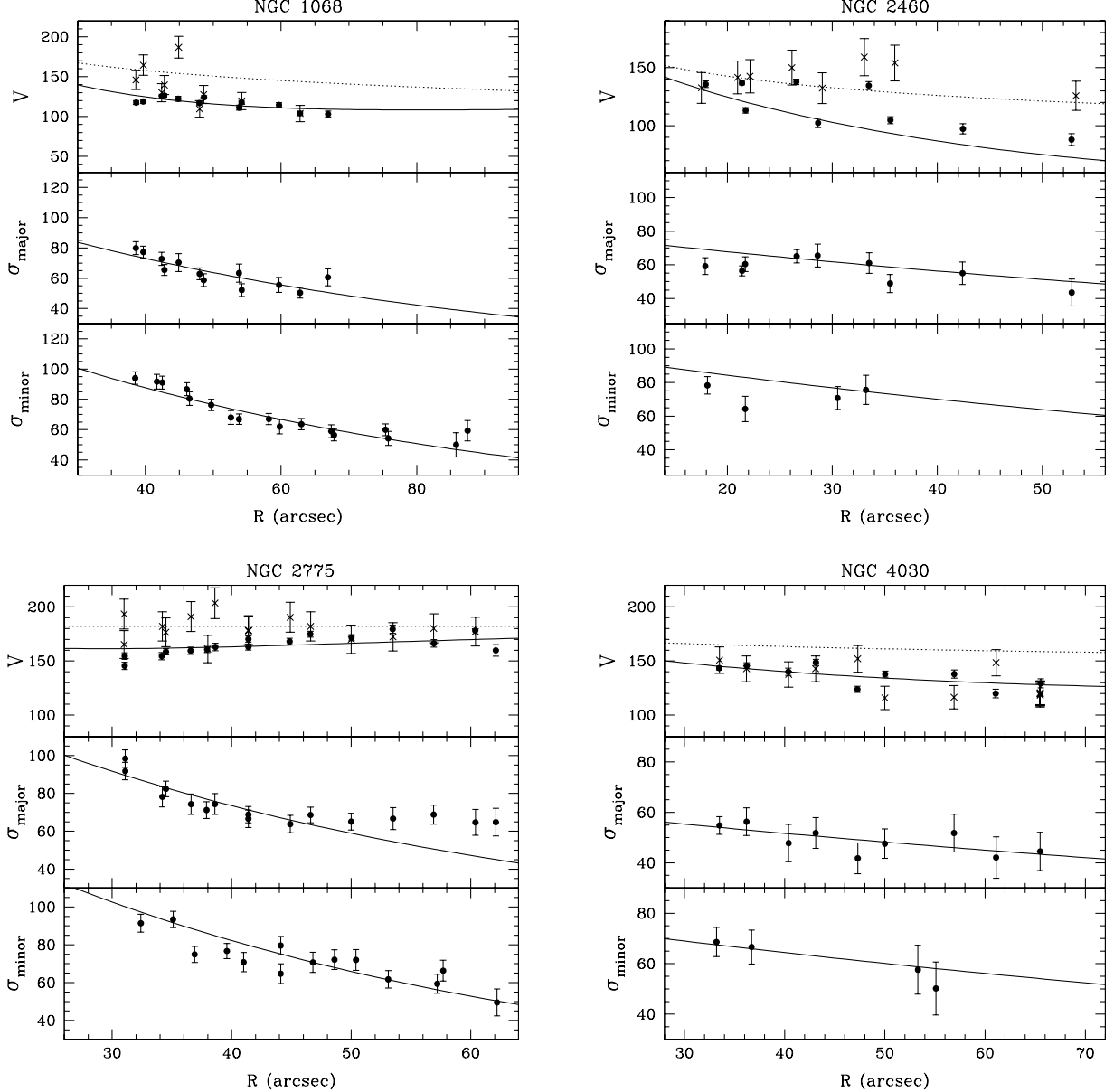


Fig. 4.— Results of fitting the model to each of the four galaxies. All kinematical quantities are in km s^{-1} . Solid points represent stellar data, and crosses represent gas kinematical data. The best-fit models for the stellar kinematics of each galaxy are shown as solid lines. The dotted lines are the circular velocities $V_c(R)$ in the models. For NGC 1068 (**a: top left**), NGC 2775 (**c: bottom left**), and NGC 4030 (**d: bottom right**), $V_c(R)$ was predicted based on the stellar rotation curve $\bar{V}(R)$ using equation (3). For NGC 2460 (**b: top right**), the gas kinematics were used to constrain $V_c(R)$.

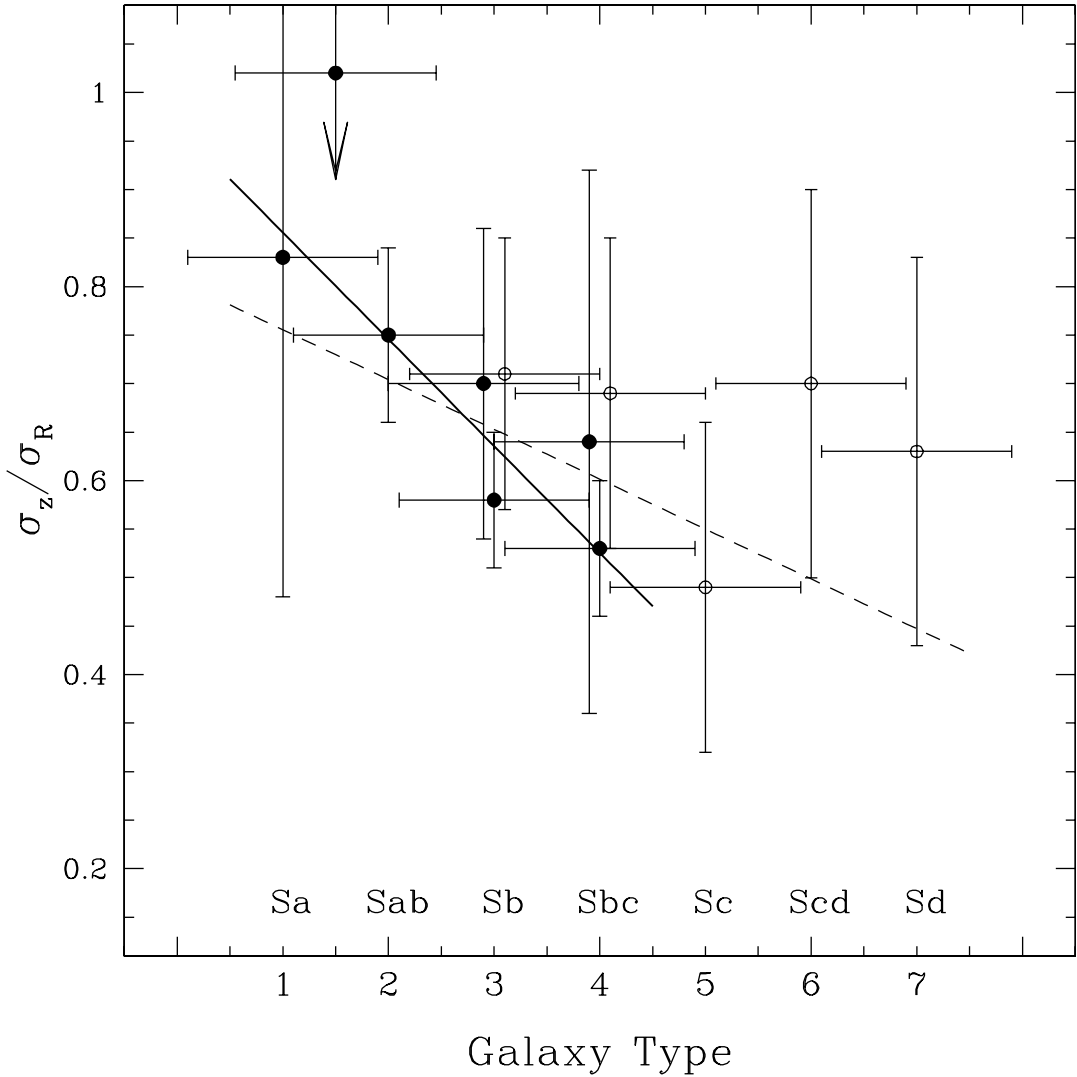


Fig. 5.— Velocity ellipsoid ratio σ_z/σ_R as a function of galactic type (Hubble stage T). The solid points displayed here represent the results obtained kinematically for individual galaxies and are best fit by the solid line. The open points represent the photometric results of van der Kruit & de Grijs (1999); when combined with our results, the data are best fit by the dashed line. Vertical error bars for our data are derived in this paper, and those for van der Kruit & de Grijs's data are statistical (the RMS of determinations for multiple galaxies of the same type). Horizontal errors represent the uncertainty inherent in galaxy classification (Naim et al. 1995). The σ_z/σ_R value for NGC 2775 is an upper limit (arrow) and was not included in the linear regression analysis.

Table 1. Galaxy Sample

Galaxy	Type	Redshift (km s ⁻¹)	Inclination (degrees)	Scale Length (arcsec)	Comments
NGC 1068	Sb	1137	30 ± 9 ^{4,5,6,7}	21 ± 3 ⁷	<i>a</i>
NGC 2460	Sa	1442	46 ± 7 ^{5,6}	15 ± 2 ⁵	<i>b</i>
NGC 2775	Sa/Sab	1354	40 ± 8 ^{2,5,9}	35 ± 7 ^{8,9}	<i>c</i>
NGC 4030	Sbc	1460	40 ± 12 ^{3,5,10}	18 ± 2 ^{1,5}	<i>b, d</i>

Note. — All redshifts and morphological classifications are from NED. The inclinations and scale lengths, unless otherwise noted, are derived using the process described in Section 3.2. Errors on the inclinations represent the spread in literature values for these quantities.

- a) The photometric scale length found here agrees with the value of 21.4 arcsec found by Laurikainen & Salo (2002) from 2MASS images.
- b) Other infrared decompositions of this galaxy were not found in the literature. Although this scale length can not be compared to other similar values, it is in keeping with available photographic decompositions of the galaxy (Grosbol 1985; Baggett et al. 1998).
- c) The scale length for NGC 2775 quoted here represents the average of two literature K band decompositions (Moriondo et al. 1998; Mollenhoff & Heidt 2001) and that done here. The error represents the total spread in these values.
- d) For NGC 4030, the isophotal ellipse method of finding the inclination was unsuccessful at arriving at a single value. The value quoted here represents the average of available literature values (Grosbol 1985; Roth 1994; Frei et al. 1996).

References:

- 1) Baggett et al. 1998
- 2) Boroson 1981
- 3) Frei et al. 1996
- 4) Garcia-Gomez et al. 2002
- 5) Grosbol 1985
- 6) Huchtmeier & Richter 1989
- 7) Laurikainen & Salo 2002
- 8) Mollenhoff & Heidt 2001
- 9) Moriondo et al. 1998
- 10) Roth 1994

Table 2. Log of Spectroscopic Observations

Galaxy	Position Angle (degrees)	Integration Time (minutes)
NGC 1068	80 - major axis	270
	170 - minor axis	210
NGC 2460	41 - major axis	240
	131 - minor axis	300
NGC 2775	168 - major axis	300
	78 - minor axis	300
NGC 4030	29 - major axis	270
	119 - minor axis	120

Note. — Major and minor axis position angles were derived from the RC3 catalog or DSS images.

Table 3. Best-fit Model Parameters

Parameter	NGC 1068	NGC 2460	NGC 2775	NGC 4030	NGC 488	NGC 2985
V_h (km s $^{-1}$)	356 ± 44	218 ± 24	283 ± 4	263 ± 51	336 ± 22	249 ± 16
α	-0.21 ± 0.03	-0.12 ± 0.15	set at 0	-0.08 ± 0.06	0.21 ± 0.04	0.18 ± 0.03
$\sigma_{R,0}$ (km s $^{-1}$)	213 ± 20	110 ± 12	197 ± 14	105 ± 23	253 ± 32	156 ± 12
$\sigma_{z,0}$ (km s $^{-1}$)	124 ± 9	92 ± 24	201 ± 14	67 ± 20	164 ± 27	117 ± 10
h_{kin} (arcsec)	72 ± 6	108 ± 55	45 ± 3	140 ± 63	38 ± 4	88 ± 13

Note. — Best-fit parameters derived from the modeling procedure. The quoted errors are one-sigma errors. For NGC 2460, the error includes systematic errors due to the asymmetric nature of the observed rotation curve (see Section 5.2). Results for NGC 488 and NGC 2985 are from improved analyses of the data presented in Gerssen et al. (1997, 2000). For NGC 488, we used fit 1 of Gerssen et al. (1997), which assumes $\sigma_{Rz}=0$, as we do for the galaxies observed here (see Section 2). For NGC 2775, α was kept fixed at zero.

Table 4. Heating in Sample Galaxies

Galaxy	Hubble Type	H ₂ Surface Density (M _⊙ pc ⁻²)	σ_z/σ_R
NGC 2460	Sa	...	0.83 ± 0.35
NGC 2775	Sa/Sab	28	$<1.02 \pm 0.11$
NGC 2985	Sab	22	0.75 ± 0.09
NGC 488	Sb	8	0.70 ± 0.16
NGC 1068	Sb	39	0.58 ± 0.07
NGC 4030	Sbc	16	0.64 ± 0.28
Milky Way	Sbc	1.8	0.53 ± 0.07

Note. — Velocity ellipsoid ratio data is from Table 3, except for the Milky Way value, which is from Hipparcos data of the solar neighborhood (Dehnen & Binney 1998). Molecular content information is estimated from CO measurements in Young et al. (1995). No CO measurements are available for NGC 2460. For the solar neighborhood, the value of the H₂ surface density is from Clemens et al. (1988).